



Effect of Post-weld Tempering on the Microstructure and Mechanical Properties in the Simulated HAZs of a High-Strength–High-Toughness Combination Marine Engineering Steel

Wen-Chao Dong¹ · Ming-Yue Wen² · Hui-Yong Pang³ · Shan-Ping Lu¹

Received: 18 May 2019 / Revised: 17 June 2019 / Published online: 10 October 2019
© The Chinese Society for Metals (CSM) and Springer-Verlag GmbH Germany, part of Springer Nature 2019

Abstract

The effects of tempering temperatures on the microstructure and mechanical properties of the simulated coarse-grain heat-affected zone (CGHAZ) and inter-critical heat-affected zone (ICHAZ) were investigated for a high-strength–high-toughness combination marine engineering steel. The results demonstrate that the microstructure of the simulated CGHAZ and ICHAZ after tempering is characterized by tempering sorbites and coarse grain in the simulated CGHAZ. As tempering temperature increases, the tensile strength of the simulated CGHAZ and ICHAZ decreases and the Charpy absorbed energy of the simulated ICHAZ at $-50\text{ }^{\circ}\text{C}$ increases remarkably, but the impact toughness of the simulated CGHAZ is not improved. After tempering at $550\text{ }^{\circ}\text{C}$, the coarse flake carbides, which distribute at the prior austenite grain and martensite lath boundaries, deteriorate the impact toughness of the simulated CGHAZ. With the increase in tempering temperature, the morphology and the size of the carbides gradually change from coarse flake to fine granular, which is beneficial to the improvement of impact toughness. However, the coarse-grain size of the simulated CGHAZ and the $M_{23}C_6$ -type carbide precipitated along the grain boundaries weakens the enhancing effect of carbides on impact toughness.

Keywords High-strength–high-toughness combination steel · Post-weld heat treatment · Heat-affected zones (HAZs) · Carbides · Impact toughness

1 Introduction

The scale of marine structures becomes more gigantic than ever before to satisfy the rapid increasing demand for ocean oil–gas resources [1, 2]. At the same time, the construction of marine structures is being extended to deeper ocean areas [3, 4]. Consequently, steels with combination of high strength and high toughness are being increasingly

used in the construction of marine engineering structures. Welding is one of the main processing technologies in the manufacture of marine engineering structures. Accordingly, it is desirable that marine engineering steels have good weldability.

It is well known that the toughness of many alloy steels with excellent strength and toughness will be deteriorated after welding thermal cycle. It is found that coarse-grain heat-affected zone (CGHAZ) and inter-critical heat-affected zone (ICHAZ), owing to the microstructure coarsening and the precipitation and growth of carbides, tend to become the local brittle zones in the heat-affected zones (HAZs) [5–10]. Post-weld heat treatment (PWHT) can not only eliminate the welding residual stress and reduce the hydrogen crack sensitivity of welded joints [11, 12], but also improve the toughness of quenched and tempered steels [13]. The precipitated carbides of different types, morphologies and sizes during tempering will affect the strength and toughness of steels. Yue et al. [14] found that using PWHT at $650\text{ }^{\circ}\text{C}$ for 1 h is beneficial to the strength recovery in the softened CGHAZ in

Available online at <http://link.springer.com/journal/40195>

✉ Shan-Ping Lu
shplu@imr.ac.cn

¹ Shenyang National Laboratory for Materials Science, Institute of Metal Research, Chinese Academy of Sciences, Shenyang 110016, China

² School of Materials Science and Engineering, University of Science and Technology of China, Shenyang 110016, China

³ Wuyang Iron and Steel Co. Ltd., Pingdingshan 462500, China

the as-welded condition for a blast-resistant steel. This is attributed to the re-precipitation of Cu-cluster and M_2C phases. The study by Wang et al. [15] showed that the impact toughness of the HAZs for 9Cr2WVTa steel is improved significantly after PWHT because the martensite lath breaks and the cell structure forms. Lee et al. [16] studied the PWHT effect on the SA508 Gr.4N steel and concluded that the deterioration of mechanical properties after PWHT is caused by the coarse $M_{23}C_6$ and M_7C_3 carbides.

Recently, a high-strength marine engineering steel with high toughness was developed by Institute of Metal Research, Chinese Academy of Sciences. The tempered martensite microstructure with additional strengthening provided by nano-scaled M_2C -type and MC -type carbides (where $M = Cr, Mo, Mn$ and V) leads to the high strength and toughness of the material. Details on the effects of tempering temperature and vanadium contents on precipitated carbides and mechanical properties can be found in publications by Wen et al. [17, 18]. It is shown in the previous research on the weldability of the steel that besides CGHAZ, some areas of the ICHAZ have poor impact toughness [19]. The main reason for the low impact energy of the CGHAZ is the formation of coarse-tempered martensite after welding thermal cycle. For the ICHAZ, the undissolved M_2C -type and MC -type carbides in the matrix promote the connection of microvoids and the formation of secondary cracks. As a result, the impact toughness of the ICHAZ is deteriorated.

In this work, tempering experiments at different tempering temperatures on the simulated CGHAZ and ICHAZ of a high-strength–high-toughness steel in marine engineering were carried out. The tensile properties (room temperature) and low-temperature Charpy absorbed energy ($-50\text{ }^\circ\text{C}$) of the simulated CGHAZ and ICHAZ after tempering were tested. Optical micrograph (OM), scanning electron microscope (SEM) and transmission electron micrograph (TEM) were used to examine the characteristic of microstructures. The statistic information of the boundary orientation distribution was obtained by electron back-scattered diffraction (EBSD) analysis. Moreover, the fracture mechanisms were investigated by observing the Charpy impact fracture surface and the longitudinal section of fractured specimens. Finally, the relationships between tempering temperature, microstructural evolution, precipitation behavior and mechanical property were discussed in detail.

2 Experimental

2.1 Materials

The chemical composition of the experimental steel for this study is listed in Table 1. The experimental steel was cut from 35-MPa super-high-pressure cylinder. A 5-pass rolling was carried out to obtain a final thickness of 12 mm using a two high 450-mm experimental hot rolling mill after homogenization at $1100\text{ }^\circ\text{C}$ for 1 h. Finally, the thick plate was subjected to the quenched and tempered procedure as $860\text{ }^\circ\text{C}/1\text{ h}/\text{air-cooled} + 860\text{ }^\circ\text{C}/40\text{ min}/\text{water-cooled} + 610\text{ }^\circ\text{C}/2\text{ h}/\text{water-cooled}$. The mechanical properties of the as-rolled plate in rolling direction were as follows: yield strength of 1135 MPa, ultimate tensile strength of 1234 MPa, elongation of 16.0%, and average impact energy of -102 J at $-50\text{ }^\circ\text{C}$.

2.2 Welding Simulation

The welding thermal cycle simulation was conducted on Gleeble 3800 thermo-mechanical simulator to investigate the microstructural evolution and mechanical property variation in the simulated CGHAZ and ICHAZ at different tempering temperatures. Two kinds of specimens with different dimensions were used in this work. The dimensions of the specimens were $11\text{ mm} \times 11\text{ mm} \times 80\text{ mm}$ for Charpy impact toughness tests and $11\text{ mm} \times 3\text{ mm} \times 80\text{ mm}$ for tensile strength tests. Two welding thermal cycle curves with the peak temperatures of $1320\text{ }^\circ\text{C}$ and $760\text{ }^\circ\text{C}$ represent the welding thermal cycle processes for the CGHAZ and ICHAZ as shown in Fig. 1. These curves were obtained by means of numerical simulation and experimental measurement [19].

2.3 Mechanical Properties

After welding thermal cycle simulation, the specimens were encapsulated in the silica tubes and tempered at $550\text{ }^\circ\text{C}$, $600\text{ }^\circ\text{C}$ and $650\text{ }^\circ\text{C}$ for 1.5 h. The $11\text{ mm} \times 3\text{ mm} \times 80\text{ mm}$ specimens were machined into the un-standard tensile specimens as shown in Fig. 2 to ensure that the fracture occurs in the uniform heated area. The tensile tests were carried out on SANS-CMT 5205 electronic universal test machine at room temperature. The block specimens were machined into the standard Charpy V-notch impact test samples with the size of $10\text{ mm} \times 10\text{ mm} \times 55\text{ mm}$ according to the standard of ASTM E23-02. The notch tip was placed in the center of simulated

Table 1 Chemical composition of the experimental steel (wt%)

| C | Ni | Cr | Mo | Mn | Si | V | S | P | Fe |
|------|------|------|------|------|------|-------|--------|-------|------|
| 0.26 | 4.08 | 0.94 | 0.72 | 0.77 | 0.12 | 0.073 | <0.001 | 0.005 | Bal. |

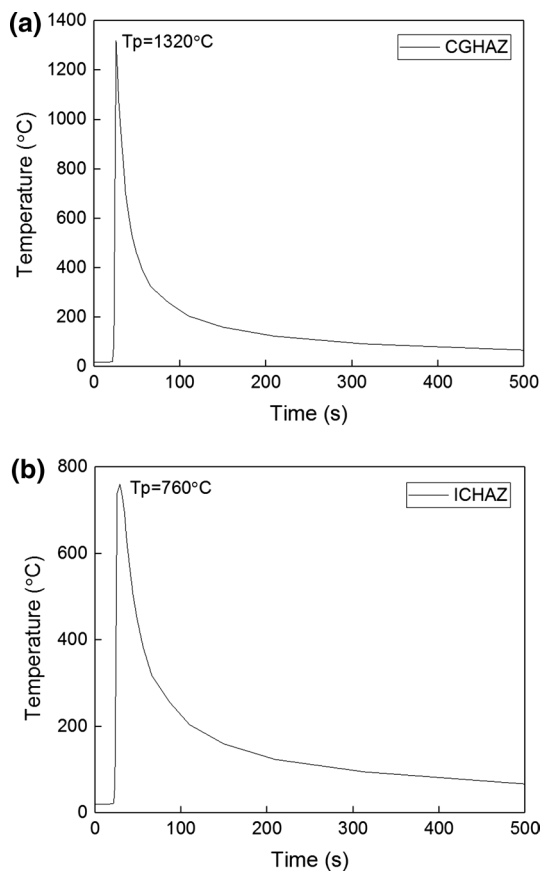


Fig. 1 Welding thermal cycles for simulated CGHAZ a, ICHAZ b

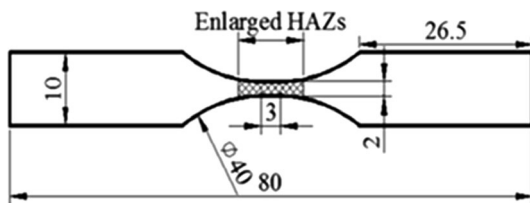


Fig. 2 Dimension figure of nonstandard tensile sample

specimens. The Charpy V-notch impact test was carried out on the SANS-ZBC-2452-C impact testing machine at -50°C .

2.4 Microstructure Observation

The specimens for optical metallography were etched by using 4% Nital solution after mechanical polishing. The microstructure was observed by Zeiss Axio Scope A1 optical microscopy (OM) and FEI QUANTA 450 scanning electron microscopy (SEM). Moreover, the impact fracture morphologies of the simulated CGHAZ and ICHAZ at different tempering temperatures were observed by FEI QUANTA 450 SEM. The EBSD specimens were electropolished in a

15 vol% perchloric acid alcohol solution at room temperature and a potential of 12 V for 30 s. The EBSD maps were acquired through SEM equipped with a HKL-Channel 5 software and a step size of $0.2\ \mu\text{m}$. Transmission electron microscope (TEM) specimens were produced by cutting slices from the specimens of the simulated CGHAZ followed by mechanical grinding to $50\ \mu\text{m}$ using SiC papers. Then, twin-jet electropolishing was conducted using a 10 vol% perchloric acid alcohol solution at -20°C and a potential of 20 V. The thin foils were examined via a FEG-TEM (FEI Tecna F20) to observe the precipitates of the simulated CGHAZ. The compositions of the precipitates were determined by energy-dispersive X-ray spectrometer (EDS) system. Moreover, the precipitated carbides of the simulated CGHAZ specimens after tempering were analyzed by means of XRD (Rigaku D/MAX-2500PC) with a scanning angle from 40° to 70° and a scanning speed of $0.2^{\circ}/\text{s}$.

3 Results

3.1 Mechanical Property

Figure 3 shows the tensile strength of the simulated CGHAZ and ICHAZ before and after tempering. It is clear that the tensile strength decreases after tempering and it exhibits decreasing trends with increasing tempering temperature. As illustrated in Fig. 4, the impact toughness of the simulated CGHAZ after tempering for 1.5 h at 550°C is lower than that in the as-welded condition. Although the impact toughness of the simulated CGHAZ could be improved by further increasing tempering temperature, no obvious improvements would be seen. On the other hand, the tempering temperature has obviously positive influence on the impact toughness of the simulated ICHAZ. The average impact energy after

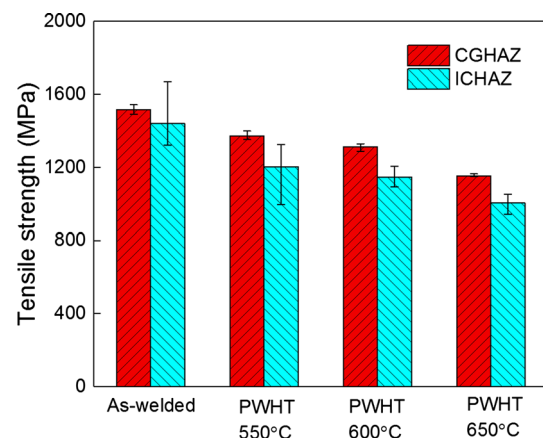


Fig. 3 Tensile strength of simulated CGHAZ and ICHAZ before and after tempering

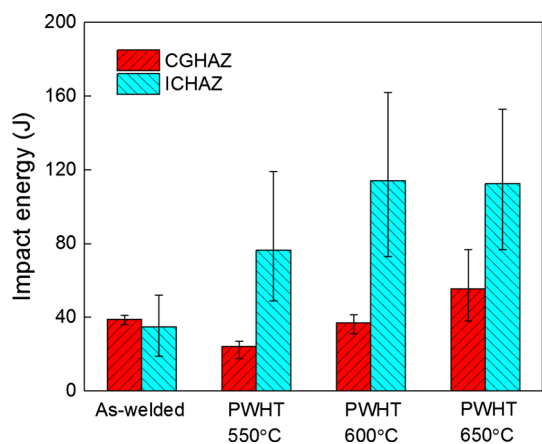


Fig. 4 Impact toughness of simulated CGHAZ and ICHAZ before and after tempering

tempering for 1.5 h at 600 °C could reach 120 J approximately, which is about three times as large as that in the as-welded condition.

3.2 Microstructural Characteristics

Figure 5 shows the optical micrographs of the simulated CGHAZ and ICHAZ before and after tempering. The peak temperature of welding thermal cycle on the simulated CGHAZ is much higher than the austenite transformation finish temperature (830 °C), which leads to the formation of coarse-quenched martensite microstructure in the simulated CGHAZ after cooling (Fig. 5a1). The mixed microstructure of quenched martensite and tempered martensite is formed in the simulated ICHAZ because the peak temperature of welding thermal cycle on the simulated ICHAZ is between the start temperature and finish temperature of austenite transformation (Fig. 5b1). After tempering, the microstructures of the simulated CGHAZ and ICHAZ are both tempered sorbites as shown in Fig. 5a2–a4 and b2–b4, respectively. Moreover, the grain size of the simulated ICHAZ is smaller than that of the simulated CGHAZ at the same tempering temperature.

Figure 6 shows the SEM images of the simulated CGHAZ and ICHAZ in the as-welded condition and after tempering. It is clear that a large number of carbides with different morphologies and sizes are precipitated in the matrix after tempering. Figure 7a shows the relationship between the precipitation temperature and the mass fraction of the carbides in the experimental steel under equilibrium state, which was calculated by Thermo-Calc software. Figure 7b presents the magnified results of Fig. 7a at 500–800 °C which is helpful for a closer examination of the precipitation and transformation of the carbides. MC -type, M_2C -type, $M_{23}C_6$ -type and M_7C_3 -type carbides will be precipitated

when the temperature is below 820 °C, and they need different temperature ranges to remain stable. For example, the temperature range for M_7C_3 -type carbides to stay stable is 500–600 °C. Furthermore, XRD was used to analyze the type of the carbides in the simulated CGHAZ after different tempering temperatures, as shown in Fig. 8. In addition to $M_{23}C_6$ -type and M_7C_3 -type carbides (Fig. 7b), there are M_3C -type carbides in the simulated CGHAZ after tempering at 550 °C as a result of the thermodynamic factors in the second-phase precipitation. $M_{23}C_6$ -type, M_7C_3 -type and M_2C -type carbides exist in the simulated CGHAZ at 600 °C, which is consistent with the calculation results of Thermo-Calc software. M_7C_3 -type carbides disappear with tempering temperature rising to 650 °C, and $M_{23}C_6$ -type, M_2C -type and MC -type carbides exist in the simulated CGHAZ.

Figure 9 shows the TEM bright-field image and selected area diffraction (SAD) pattern on the precipitated carbides found in the simulated CGHAZ after tempering. The chemical composition of the carbides was determined by EDS. The diffraction pattern and the chemical composition of the carbides were analyzed to identify the types of the carbides. At different tempering temperatures, there are granular $M_{23}C_6$ -type carbides (with length of 100–200 nm) along the martensite lath or prior austenite grain boundaries. After tempering at 550 °C, the coarser flake M_3C -type carbides precipitate along the prior austenite grain boundaries (with length of 500 nm). Moreover, there are finer acicular M_7C_3 -type carbides (with length of 250–300 nm) inside the martensite lath. When tempering temperature is 600 °C, in addition to acicular M_7C_3 -type carbides, there are finer acicular M_2C -type carbides (with length of 100–150 nm) inside the martensite lath. After tempering at 650 °C, the finer granular MC -type carbides (~50 nm) and the acicular M_2C -type carbides are observed, but the acicular M_7C_3 -type carbides disappear. The type, morphology, dimension and chemical composition of each kind of carbides in the simulated CGHAZ specimens are listed in Table 2.

3.3 Crystallographic Characteristics

The crystallographic characteristics of the simulated CGHAZ after tempering at 550 °C and 650 °C were analyzed by EBSD and are presented in Fig. 10, respectively. In general, 15° can be defined as the critical angle of the high- and low-angle grain boundary [20, 21]. As shown in Fig. 10, the white lines represent the low misorientation boundaries of 2°–3° and the black lines stand for the high misorientation boundaries of no less than 15°. The martensite lath packets and the prior austenite grain boundaries show the characteristics of high orientation difference, while the boundaries of sub-blocks in the packet show those of low orientation difference. A simple statistics on the number fraction of the misorientation

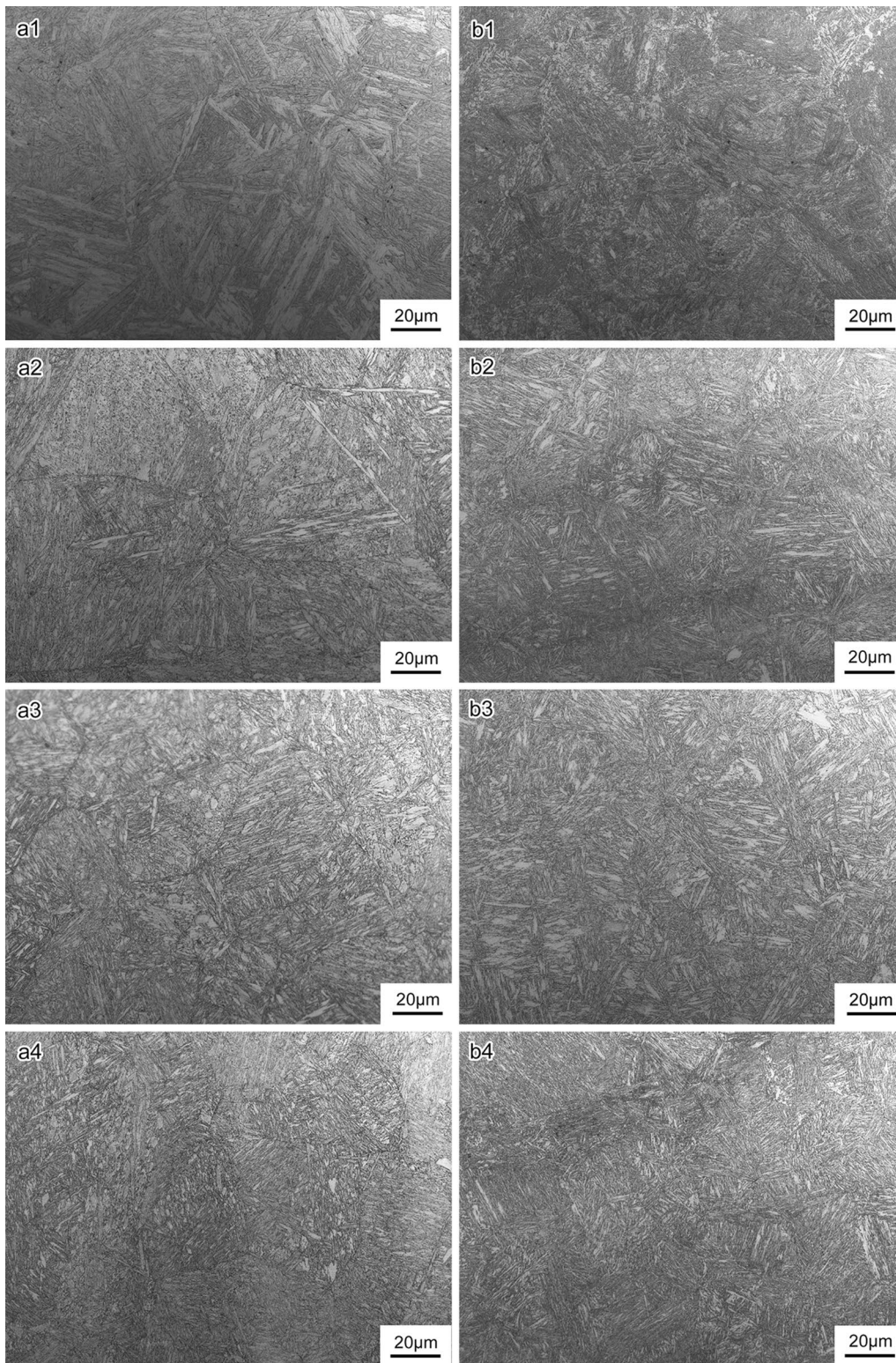


Fig. 5 Optical micrographs of simulated CGHAZ **a1** as-welded, **a2** PWHT 550 °C, **a3** PWHT 600 °C, **a4** PWHT 650 °C, and ICHAZ **b1** as-welded, **b2** PWHT 550 °C, **b3** PWHT 600 °C, **b4** PWHT 650 °C

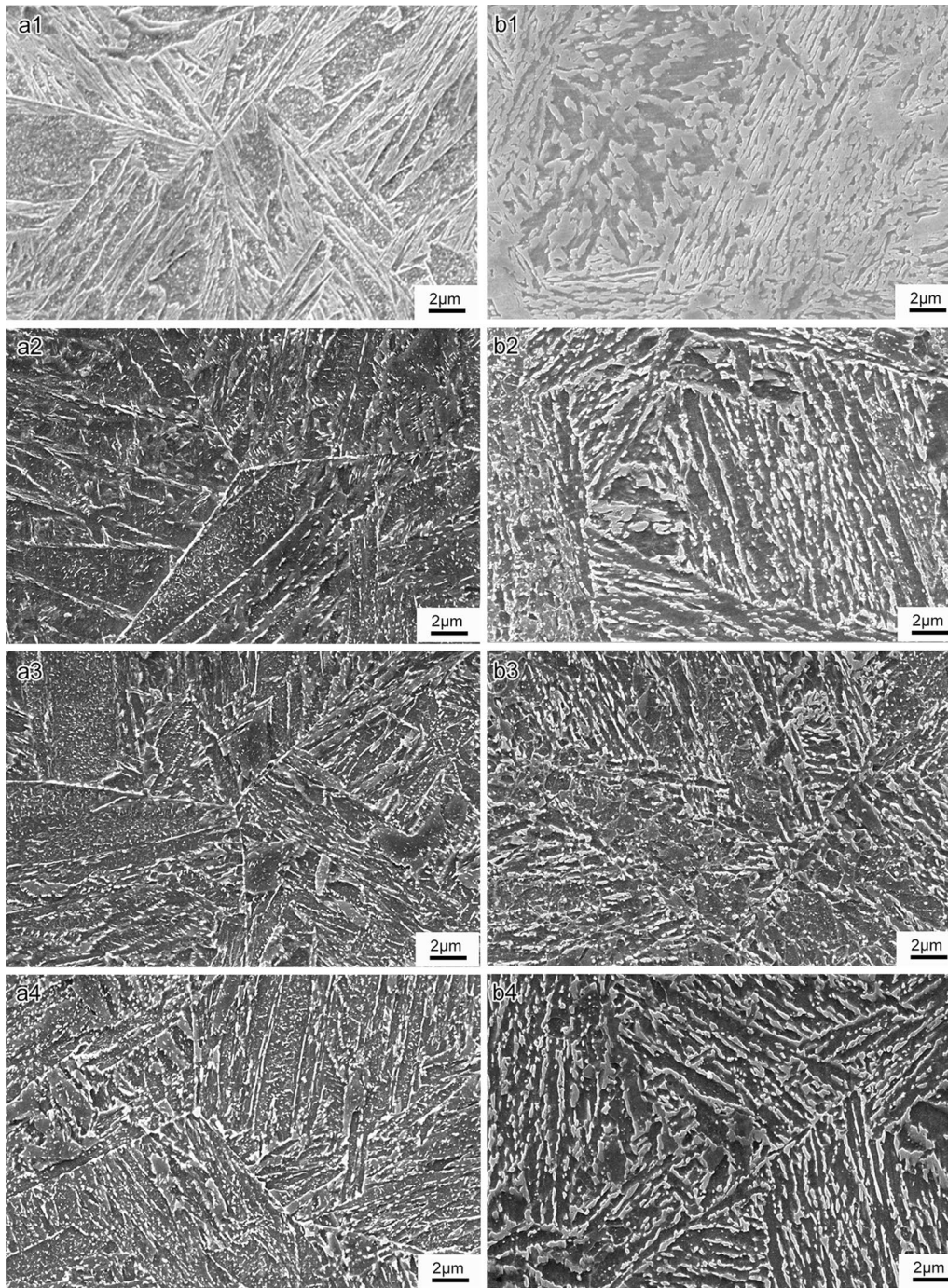


Fig. 6 SEM images of simulated CGHAZ **a1** as-welded, **a2** PWHT 550 °C, **a3** PWHT 600 °C, **a4** PWHT 650 °C, ICHAZ **b1** as-welded, **b2** PWHT 550 °C, **b3** PWHT 600 °C, **b4** PWHT 650 °C

distribution from the two specimens is summarized in Fig. 11. It can be seen that the number fraction of the high misorientation angle ($> 15^\circ$) increases from 12.7 to 15.0% with the increase in the tempering temperature from 550 to 650 °C. The studied results show that the low-angle grain boundary can effectively hinder the slip of dislocation, while the high-angle grain boundary can effectively

inhibit the growth of cleavage cracks [22–24]. Therefore, the impact toughness of the simulated CGHAZ after tempering at 650 °C should be better than that at 550 °C.

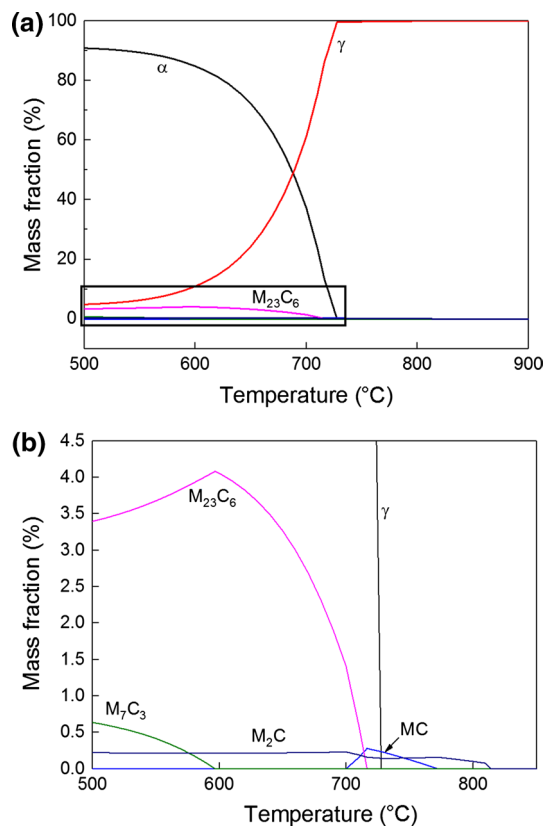


Fig. 7 Mass fraction of phases in the experimental steel under equilibrium state as a function of temperature: **a** whole diagram, **b** partial diagram

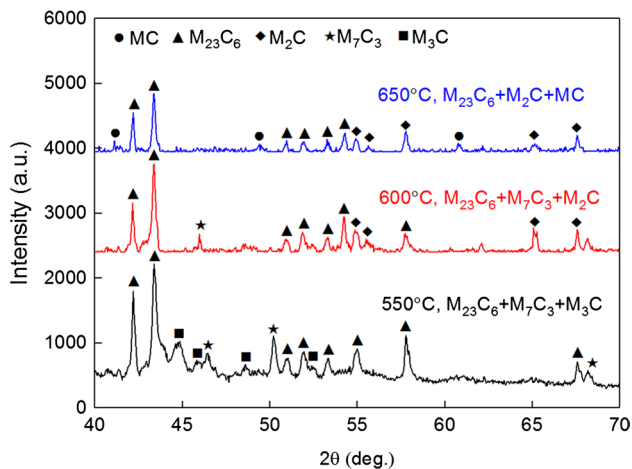


Fig. 8 XRD spectra of carbides with different tempering temperatures in simulated CGHAZ

4 Discussion

After tempering, the lath martensite microstructure is broken and transformed into lath ferrite matrix and carbide

precipitates. Ferrites have lower strength compared with martensites. Consequently, the tensile strength of the simulated CGHAZ and ICHAZ is lower than that before tempering. With the increase in tempering temperature, the substructures inside the lath martensite recover dynamically and the low-angle grain boundaries decrease gradually, which leads to the reducing barriers to dislocation motion and the decrease in tensile strength.

Previous studies [25, 26] have shown that both martensite packet and block boundaries are high-angle grain boundary. In the process of crack propagation, a high-angle transition will occur when the crack encounters the high-angle grain boundary. With the increase in the number of high-angle interface, that of crack turning will increase, more energy will be consumed in the process of crack propagation, and the impact toughness will be improved. Therefore, the change of the size of the packet and the block plays a decisive role in toughness and can be used as “effective grain size” to control toughness. As the effective grain size decreases, the high-angle grain interface required for crack propagation increases, which consumes more energy and has higher impact energy. Compared with the simulated CGHAZ with coarse grains, the simulated ICHAZ has smaller grains and no obvious growth after tempering (Figs. 5 and 6). Therefore, the impact toughness of the simulated ICHAZ after tempering is greatly improved as shown in Fig. 4. However, for the simulated CGHAZ, the impact toughness at 550 °C is lower than that before tempering, while the impact toughness is not significantly improved at 600 °C and 650 °C.

The impact fracture morphology and the microstructure near the fracture were examined to investigate the temper embrittlement mechanism of the simulated CGHAZ at 550 °C. The fracture initiation and propagation zones in a Charpy impact fracture surface for a tempered martensite steel were defined by Zia-Ebrahimi et al. [27, 28], as shown schematically in Fig. 12. Figures 13 and 14 show the low- and high-magnification fractographs of Charpy impact specimens of the simulated CGHAZ and ICHAZ at -50 °C before and after tempering, respectively. After tempering, the stable crack propagation zone and the shear lip are found in the fracture surface of the simulated ICHAZ, which exhibits the characteristics of dimple fracture (Figs. 13b2–b4 and 14b2–b4). At tempering temperatures of 600 °C and 650 °C especially, there are a lot of larger and deeper dimples in the fracture surface, which shows an excellent toughness in the simulated ICHAZ. The impact fracture morphology of the simulated CGHAZ in all conditions is dramatically different, and the fracture mode has also changed significantly. Before tempering, the fracture surface of the simulated CGHAZ presents quasi-cleavage fracture (Figs. 13a1 and 14a1). However, the impact fracture surface after tempering at 550 °C and

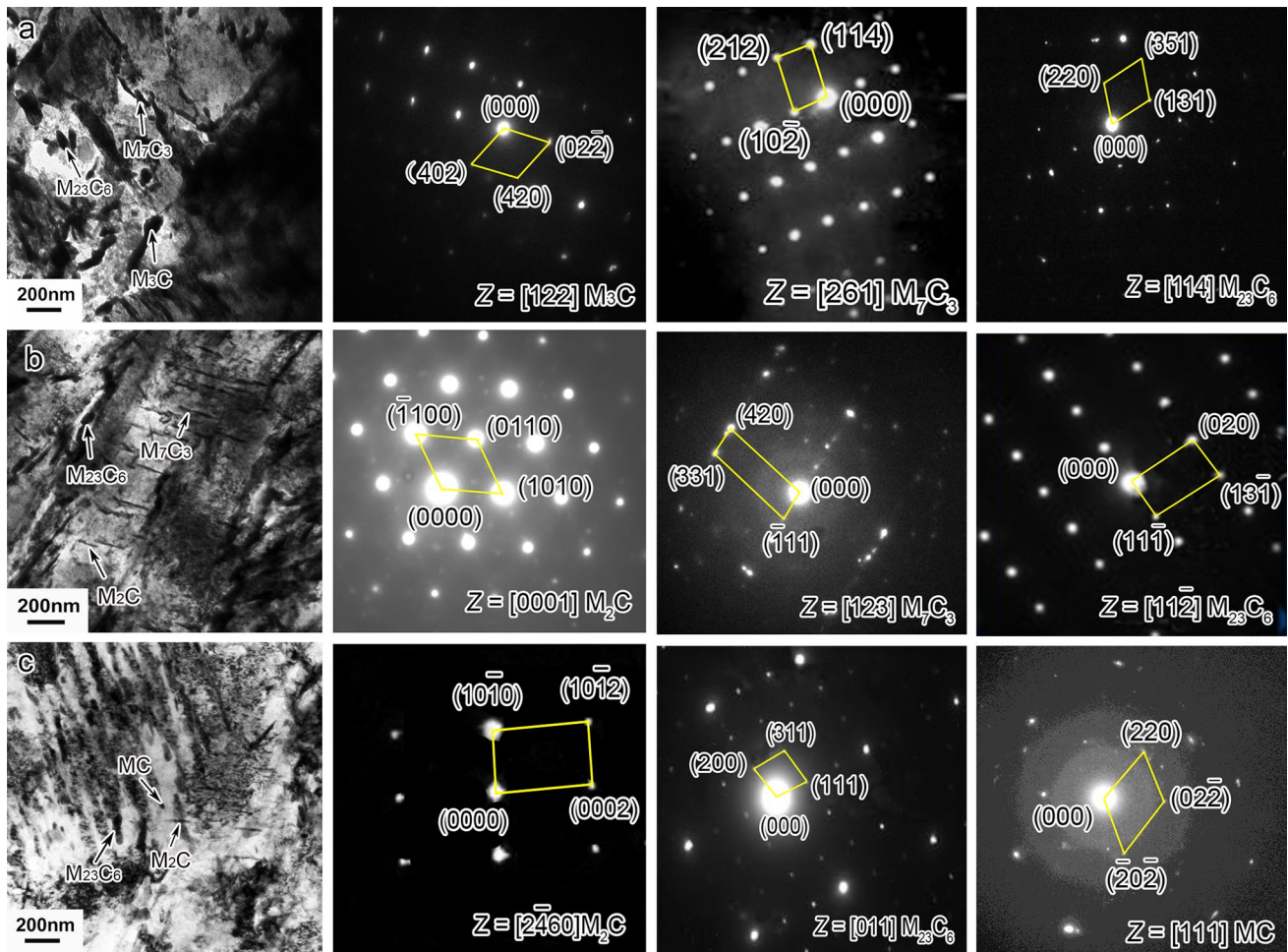


Fig. 9 TEM bright-field images and selected area diffraction (SAD) patterns of the precipitated carbides in simulated CGHAZ after tempering for 1.5 h at 550 °C **a**, 600 °C **b**, 650 °C **c**

Table 2 Type, morphology, dimension and chemical composition of carbides in the simulated CGHAZ at different tempering temperatures

| Temperature (°C) | Carbide type | Dimension (nm) | Alloying elements | Morphology |
|------------------|--------------|----------------|-------------------|------------|
| 550 | M_3C | ~ 500 | Fe Cr | Flake |
| | $M_{23}C_6$ | 80–120 | Fe Cr | Granular |
| | M_7C_3 | 250–300 | Fe Mo | Acicular |
| 600 | M_7C_3 | 250–300 | Fe Mo | Acicular |
| | $M_{23}C_6$ | 80–120 | Fe Cr | Granular |
| | M_2C | 150–200 | Fe Mo | Acicular |
| 650 | M_2C | 100–150 | Fe Mo | Acicular |
| | $M_{23}C_6$ | 80–120 | Fe Cr | Granular |
| | MC | ~ 50 | Mo V | Granular |

600 °C shows a feature of brittle fracture with mainly an unstable crack propagation zone (Figs. 13a2, a3 and 14a2, a3). After tempering at 650 °C, the proportion of the stable crack propagation zone in the fracture surface increases, which is typical of quasi-cleavage fracture (Figs. 13a4 and

14a4). The microstructure near the fracture in the simulated CGHAZ after tempering at 550 °C and 650 °C was also examined as shown in Fig. 15. It can be seen that numerous microvoids and microcracks are observed near the fracture. Almost all of the microvoids observed in the

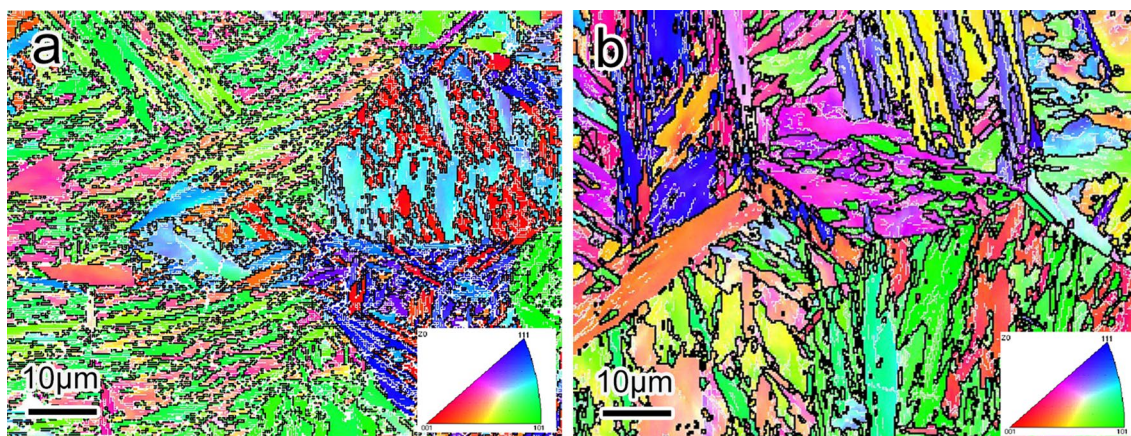


Fig. 10 EBSD images of simulated CGHAZ after tempering for 1.5 h at 550 °C a, 650 °C b

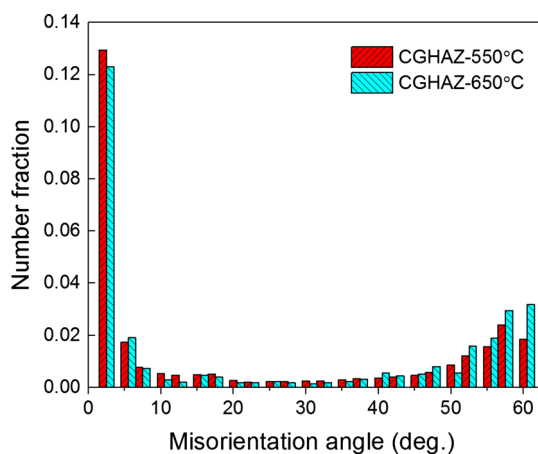


Fig. 11 Number fraction with different misorientations for simulated CGHAZ after tempering for 1.5 h at 550 °C and 650 °C

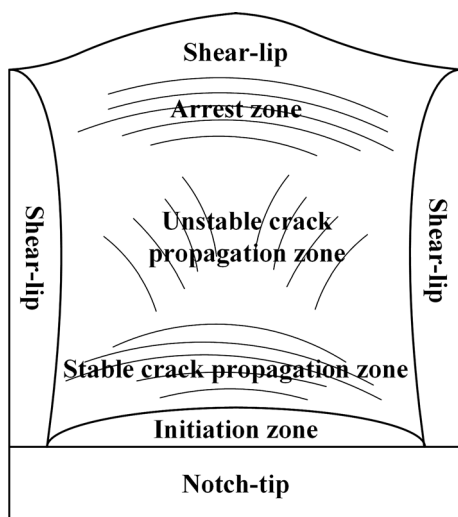


Fig. 12 Schematic diagram in the fracture surface of Charpy impact specimen

specimens are circular. The microvoids and microcracks mainly distribute along the prior austenite grain or martensite lath boundaries. The size of the microvoids and microcracks at 550 °C is larger than that at 650 °C.

While tempered sorbite can be detected after tempering at different temperatures, the type, morphology, size and distribution of carbides are different, resulting in significant differences in impact absorbed energy. The coarse flake M_3C -type carbides mainly precipitate along the prior austenite grain or martensite lath boundaries after tempering for 1.5 h at 550 °C. The stress in the matrix is always concentrated when the flake carbides are subjected to external stress during impact deformation, which results in the brittle fracture of flake carbides and the forming of microcracks. The cracks produced at the coarse flake M_3C -type carbides are easily connected with each other along the chains of the carbides, as shown in Fig. 15a, which promotes crack propagation. Therefore, the fractures tend to occur in the cleavage mode (Figs. 13a2 and 14a2). This decreases the impact adsorbed energy and leads to temper embrittlement. In terms of the microscopic fracture morphology (Fig. 14a2, a3), the area of the cleavage surface at 600 °C is smaller than that at 550 °C. In addition, there is a necklace-like white fracture zone around the area constituting the cleavage surface. The white fracture zone is composed of many small dimples. It can be inferred that ductile fracture occurs around cleavage fracture surface during impact process [29]. Therefore, the impact toughness is improved slightly, which is due to the reduction of coarse flake carbides after tempering at 600 °C. After tempering at 650 °C, the coarse flake carbides almost completely disappear. There are only a small amount of acicular M_2C -type carbides and finer granular MC -type carbides in the matrix. The decrease in the amount of coarse flake carbides and the change in carbide morphology bring about a reduction

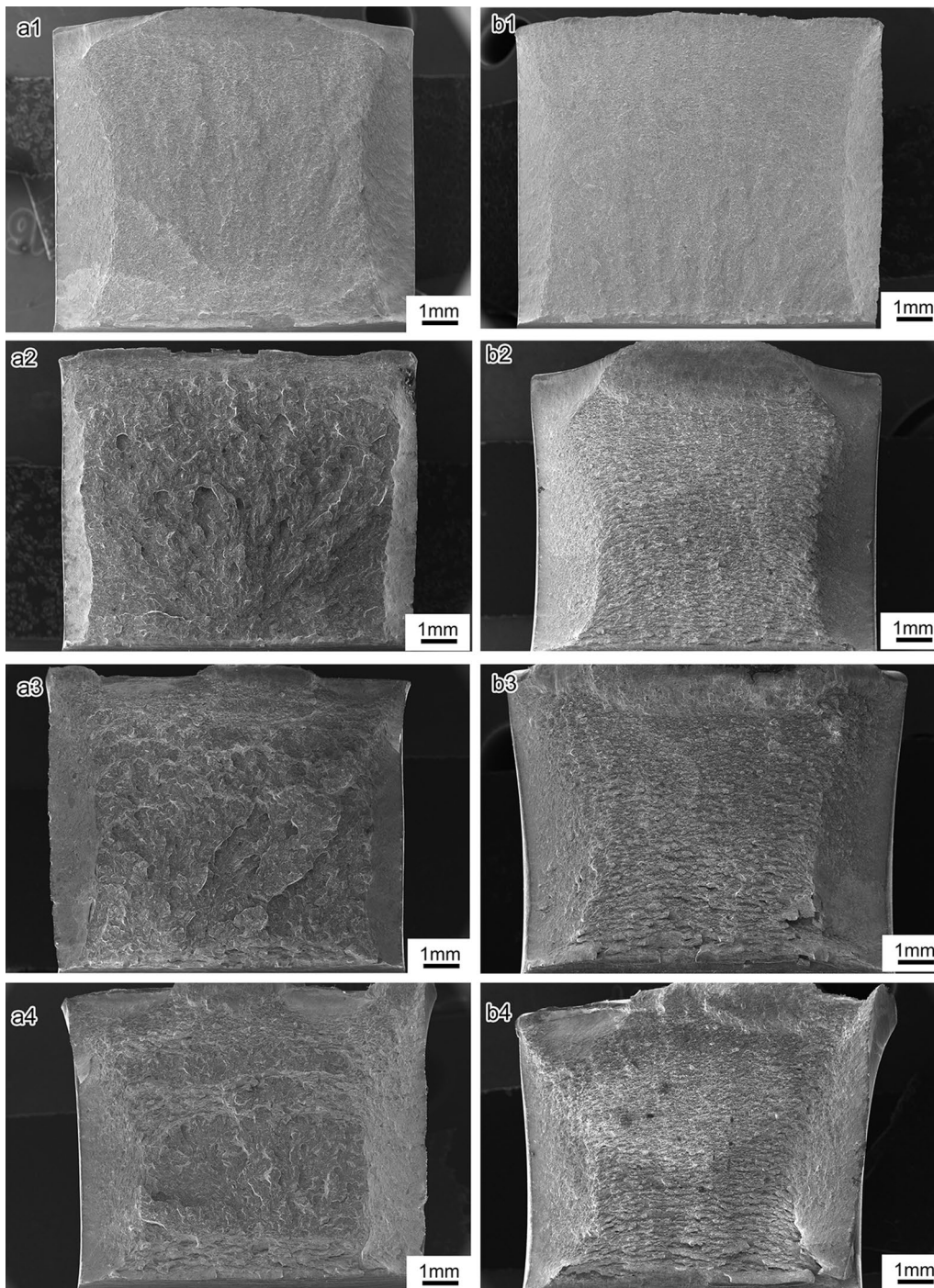


Fig. 13 SEM low-magnification fractographs of Charpy impact specimens at $-50\text{ }^{\circ}\text{C}$ in simulated CGHAZ **a1** as-welded, **a2** PWHT $550\text{ }^{\circ}\text{C}$, **a3** PWHT $600\text{ }^{\circ}\text{C}$, **a4** PWHT $650\text{ }^{\circ}\text{C}$, and ICHAZ **b1** as-welded, **b2** PWHT $550\text{ }^{\circ}\text{C}$, **b3** PWHT $600\text{ }^{\circ}\text{C}$, **b4** PWHT $650\text{ }^{\circ}\text{C}$

in stress concentration, an increase in the initiation work of microcracks during impact process and an improvement in the impact toughness of the simulated CGHAZ. On the other hand, because of the coarse-grain size of the simulated CGHAZ and the $M_{23}C_6$ -type carbides precipitated along the grain boundaries, the improvement

of impact toughness is weakened. As a result, no obvious improvements can be found in the impact toughness of the simulated CGHAZ. It can be observed that there are stable crack propagation zones in the fracture surface (Fig. 13a4), and the area of the white ductile fracture zone is larger than that at $600\text{ }^{\circ}\text{C}$ (Fig. 14a4).

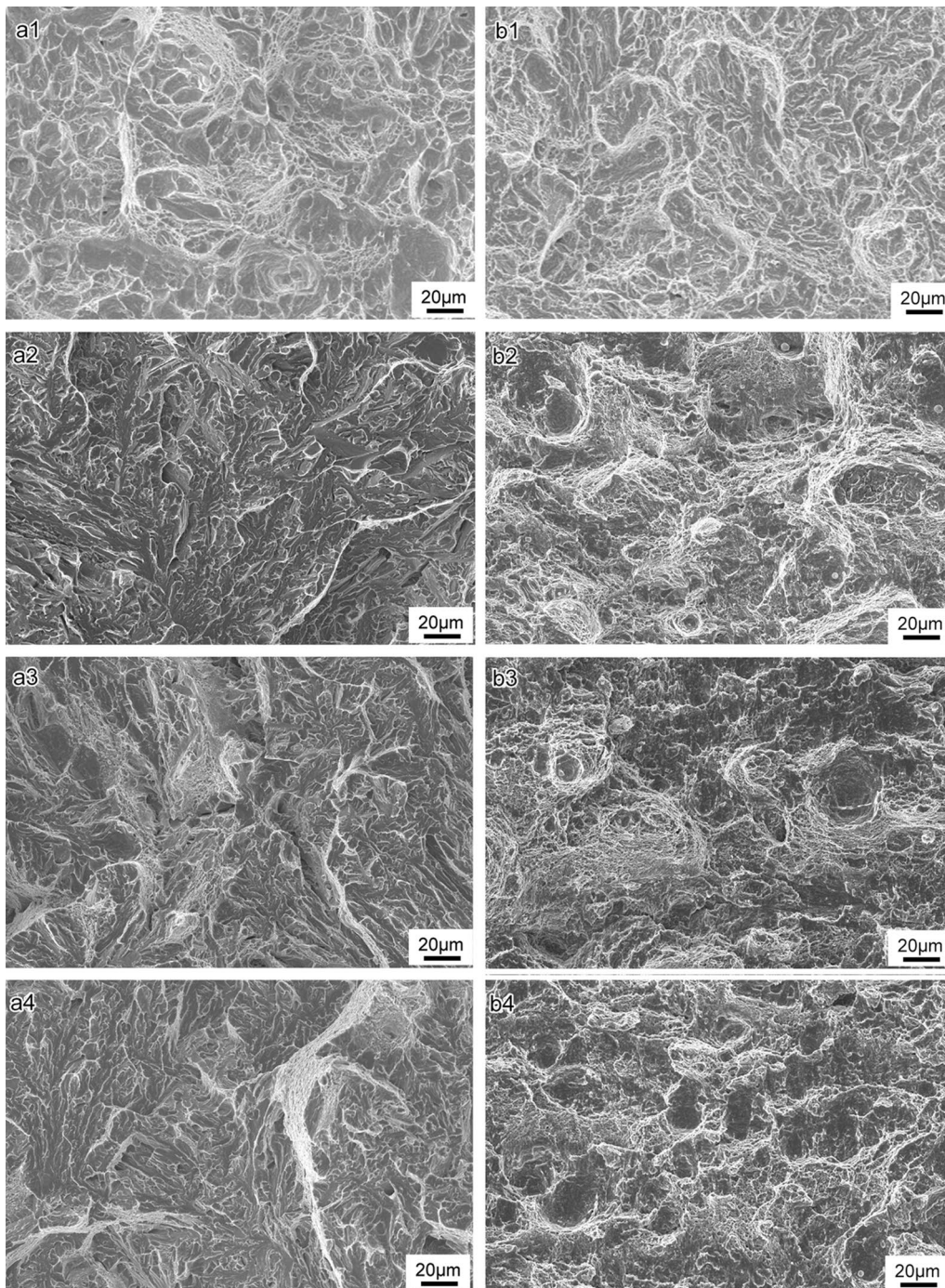


Fig. 14 SEM high-magnification fractographs of Charpy impact specimens at $-50\text{ }^{\circ}\text{C}$ in simulated CGHAZ **a1** as-welded, **a2** PWHT $550\text{ }^{\circ}\text{C}$, **a3** PWHT $600\text{ }^{\circ}\text{C}$, **a4** PWHT $650\text{ }^{\circ}\text{C}$, and ICHAZ **b1** as-welded, **b2** PWHT $550\text{ }^{\circ}\text{C}$, **b3** PWHT $600\text{ }^{\circ}\text{C}$, **b4** PWHT $650\text{ }^{\circ}\text{C}$

5 Conclusions

The changes in the microstructure and mechanical properties of the simulated CGHAZ and ICHAZ for a high-strength–high-toughness steel in marine engineering at different tempering temperatures were studied. The major conclusions are summarized as follows:

1. Tempering temperature decreases the tensile strength of the simulated CGHAZ and ICHAZ and improves the low-temperature impact toughness of the simulated ICHAZ, but there is no obvious improvement in low-temperature impact toughness of the simulated CGHAZ.
2. After tempering, both the simulated CGHAZ and ICHAZ are tempered sorbites, but the grains of the

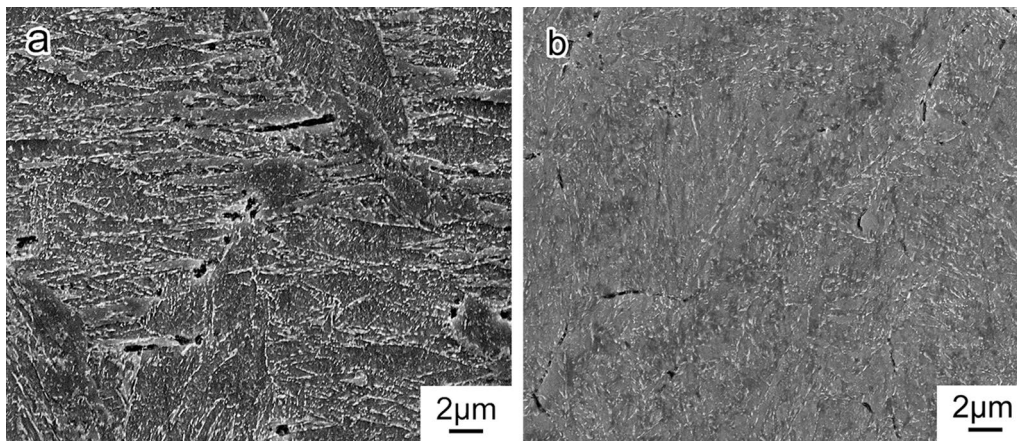


Fig. 15 SEM micrographs near the fracture of simulated CGHAZ specimens after tempering for 1.5 h at 550 °C **a**, 650 °C **b**

simulated CGHAZ are relatively coarse. Carbides of different types and sizes with different morphologies and distributions are precipitated in the matrix and affect the impact toughness of the simulated CGHAZ.

3. After tempering at 550 °C, the coarse flake M_3C -type carbides are precipitated along the prior austenite grain or martensite lath boundaries in the simulated CGHAZ. The carbides cause the brittle fracture or form the microcracks during impact process and deteriorate the impact toughness of the simulated CGHAZ. With the increase in tempering temperature, the morphology and the size of the carbides gradually change from coarse flake to fine granular, which is beneficial to the improvement in impact toughness. However, the coarse-grain size of the simulated CGHAZ and the $M_{23}C_6$ -type carbides precipitated along the grain boundaries weakens the enhancing effect of the carbides on the impact toughness. The impact toughness of the simulated ICHAZ is dramatically improved due to the smaller grain size.

Acknowledgements The authors gratefully acknowledge the financial support of the sponsor from the National Key Research and Development Program of China (No. 2016YFB0300601) and the Key Programs of Chinese Academy of Sciences (No. GFZD-125-15-003-1).

References

- [1] D. Liu, Q. Li, T. Emi, *Metall. Mater. Trans. A* **42**, 1349 (2011)
- [2] Y.L. Zhou, Y. Xu, J. Chen, Z.Y. Liu, *Acta Metall. Sin.* **47**, 11 (2011)
- [3] H.C. Ma, Z.Y. Liu, C.W. Du, H.R. Wang, X.G. Li, D.W. Zhang, Z.Y. Cui, *Corros. Sci.* **100**, 627 (2015)
- [4] X. He, R.G. Song, D.J. Kong, *J. Alloys Compd.* **770**, 771 (2019)
- [5] Y.W. Shi, Z.X. Han, *J. Mater. Process. Technol.* **207**, 30 (2008)
- [6] L.Y. Lan, C.L. Qiu, D.W. Zhao, X.H. Gao, L.X. Du, *Mater. Sci. Eng. A* **529**, 192 (2011)
- [7] P.S. Zhou, B. Wang, L. Wang, Y.W. Hu, L. Zhou, *Mater. Sci. Eng. A* **722**, 112 (2018)
- [8] S. Kumar, S.K. Nath, *J. Mater. Process. Technol.* **236**, 216 (2016)
- [9] H. Xie, L.X. Du, J. Hu, G.S. Sun, H.Y. Wu, R.D.K. Misra, *Mater. Sci. Eng. A* **639**, 482 (2015)
- [10] E.J. Barrick, J.N. DuPont, *Mater. Sci. Eng. A* **748**, 189 (2019)
- [11] P.S. Dong, S.P. Song, J.M. Zhang, *Int. J. Press. Vessels Pip.* **122**, 6 (2014)
- [12] J.G. Nawrocki, J.N. DuPont, C.V. Robino, A.R. Marder, *Metall. Mater. Trans. A* **32**, 2585 (2001)
- [13] M. Divya, C.R. Das, V. Ramasubbu, S.K. Albert, A.K. Bhaduri, *J. Mater. Process. Technol.* **211**, 2032 (2011)
- [14] X. Yue, X.L. Feng, J.C. Lippold, *Mater. Sci. Eng. A* **585**, 149 (2013)
- [15] J. Wang, S.P. Lu, L.J. Rong, D.Z. Li, *J. Nucl. Mater.* **470**, 1 (2016)
- [16] K.H. Lee, M.J. Chung, M.C. Kim, B.S. Lee, *Nucl. Eng. Technol.* **46**, 413 (2014)
- [17] T. Wen, X.F. Hu, Y.Y. Song, D.S. Yan, L.J. Rong, *Mater. Sci. Eng. A* **588**, 201 (2013)
- [18] T. Wen, X.F. Hu, Y.Y. Song, D.S. Yan, L.J. Rong, *Acta Metall. Sin.* **50**, 447 (2014)
- [19] M.Y. Wen, W.C. Dong, H.Y. Pang, S.P. Lu, *Acta Metall. Sin.* **54**, 501 (2018)
- [20] M. Díaz-Fuentes, A. Iza-Mendia, I. Gutiérrez, *Metall. Mater. Trans. A* **34**, 2505 (2003)
- [21] Z.R. Shi, C.F. Yang, R.Z. Wang, H. Su, F. Chai, J.F. Chu, Q.F. Wang, *Mater. Sci. Eng. A* **649**, 270 (2016)
- [22] A. Lambert-Perlade, A.F. Gourgues, A. Pineau, *Acta Mater.* **52**, 2337 (2004)
- [23] A.F. Gourgues, *Mater. Sci. Technol.* **18**, 119 (2002)
- [24] H. Kitahra, R. Ueji, N. Tsuji, Y. Minamino, *Acta Mater.* **54**, 1279 (2006)
- [25] C.F. Wang, M.Q. Wang, J. Shi, W.J. Hui, H. Dong, *Scr. Mater.* **58**, 492 (2008)
- [26] X.Y. Wang, T. Pan, H. Wang, H. Su, X.Y. Li, X.Z. Cao, *Acta Metall. Sin.* **48**, 401 (2012)
- [27] F. Zia-Ebrahimi, G. Krauss, *Acta Metall.* **32**, 1767 (1984)
- [28] H. Kim, J. Park, M. Kang, S. Lee, *Mater. Sci. Eng. A* **649**, 57 (2016)
- [29] P. Wang, S.P. Lu, N.M. Xiao, D.Z. Li, Y.Y. Li, *Mater. Sci. Eng. A* **527**, 3210 (2010)